The role of plastic strains on variant selection in ausformed bainitic microstructures studied by finite elements and crystal plasticity simulations

Eres-Castellanos, Adriana; Hidalgo, Javier; Morales-Rivas, Lucia; Caballero, Francisca G.; Garcia-Mateo, Carlos

DOI
10.1016/j.jmrt.2021.05.070

Publication date
2021

Document Version
Final published version

Published in
Journal of Materials Research and Technology

Available online at www.sciencedirect.com

jmr&t Journal of Materials Research and Technology

journal homepage: www.elsevier.com/locate/jmrt

Original Article

The role of plastic strains on variant selection in ausformed bainitic microstructures studied by finite elements and crystal plasticity simulations

Adriana Eres-Castellanos [a], *Javier Hidalgo* [b], *Lucia Morales-Rivas* [c], *Francisca G. Caballero* [a], *Carlos Garcia-Mateo* [a,*]

[a] *Department of Physical Metallurgy, National Center for Metallurgical Research (CENIM-CSIC), Gregorio del amo 8, 28040, Madrid, Spain*

[b] *Delft University of Technology, Materials Science and Engineering, Mekelweg 5, Delft 2628, Netherlands*

[c] *Materials Testing, University of Kaiserslautern, Gottlieb-Daimler-Straße, 67663 Kaiserslautern, Germany*

ARTICLE INFO

Article history:
Received 25 January 2021
Accepted 24 May 2021
Available online 29 May 2021

Keywords:
Bainite
Thermomechanical treatment
Ausforming
Texture
Anisotropy
Variant selection

ABSTRACT

The mechanisms driving variant selection phenomena in ausformed bainitic microstructures are not fully controlled yet. Previous results are not congruent among them, as they cannot be explained by the same rule. In this work, we aimed to understand the mechanisms governing variant selection in a medium carbon-high silicon steel subjected to ausforming treatments. To do so, the microstructural characterization in different regions of barreled samples has been combined with the simulation of the stress and strain state at the macro and micro level, by finite elements simulations and crystal plasticity simulations, respectively. The main conclusion is that the variant selection shown in these microstructures can be explained by understanding the distribution of the plastic strains at the macro and micro level. The selection of crystallographic variants is more pronounced in the regions which have been more deformed. Also, the deformation distributes along deformation microbands, where the most promoted variants seem to grow, in good agreement with previous results in ausformed lath martensite.

1. Introduction

Ausforming treatments are an alternative way to obtain bainite. In these treatments, the austenite is plastically deformed before the bainitic transformation starts [1]. This may lead to many benefits, e.g. the acceleration of the transformation or the refinement of the microstructure [1,2] and to some drawbacks. For instance, the austenite can get stabilized because of the increase of the dislocation density. However, if the retained austenite is not stable enough, it could transform to martensite in the first stages of the deformation during mechanical testing, being detrimental for the mechanical properties [3–5]. Also, the application of deformation is associated to the formation of strain induced phases – phases induced above the austenite yield strength by the effect of the

* Corresponding author.
E-mail address: cgm@cenim.csic.es (C. Garcia-Mateo).

https://doi.org/10.1016/j.jmrt.2021.05.070

stress - during the deformation step, where these strain induced phases can be coarse bainite or martensite and may affect the mechanical properties [6]. Finally, the plastic deformation of austenite is also linked to variant selection phenomena, which is associated to the coarsening of the bainitic ferrite crystallographic blocks and, thus, to the worsening of the fatigue properties of the microstructure [2,7–9].

The mechanisms driving variant selection in bainitic ferrite are not fully controlled. A microstructure is said to undergo variant selection if, depending on the orientation relationship (OR), there are less than 24 or 12 orientations of bainitic ferrite in every single prior austenite grain. Variant selection can affect the mechanical properties, as it is associated to the increase of area of crystallographic blocks and packages of bainitic ferrite [1] and to the decrease of the amount of austenite blocks in the microstructure [10]. Gong et al. [7] studied the variant selection phenomena in a high carbon-high silicon steel subjected to ausforming treatments and concluded that the phenomena could be explained by using a rule that focuses on Shockley partial dislocations. However, some of the authors of this work [11] showed that the mentioned rule could not explain the variant selection phenomena reported in a medium carbon-high silicon steel subjected to ausforming treatments. Although the obtained results suggested that variants were selected by a rule which involved the application of stress and/or strain, the most reported variants did not comply with the ones predicted by the model. In this work, we aim to understand the mechanisms driving variant selection in that medium carbon-high silicon steel under the same ausforming treatments than in Ref. [11]. To do so, we have characterized different regions in the samples of study. Because samples undergo a barreling effect due to the compression step in the ausforming treatments, the stress and strain states are not the same in different regions of the sample. The comparison of some microstructural features, combined with the simulation of the stress and strain state at the macro and micro level - by Finite Elements (FE) simulations and crystal plasticity simulations, respectively - have enabled us to better understand the bainitic transformation from plastically deformed austenite.

2. Experimental and simulation methods

The commercial steel SCM40 used in this study is produced by Sidenor and is a medium C (0.4 wt.%) high Si (3 wt.%) steel, which also contains Cr and Mo for industrial process purposes.

Tests were performed in a Bahr 805D high-resolution dilatometer in which the temperature was controlled by a type K thermocouple welded to the central part of the sample surface. The dilatometer was equipped with an induction heating coil to increase the temperature and helium was used to decrease it. The equipment enables to simulate thermal and thermomechanical treatments and measure the longitudinal change in length of the samples to study phase transformations. The dilatometry tests were performed using a module equipped with fused silica push-rods and the compression tests were carried out by using a deformation module with silicon nitride punchers. The punchers were separated from the samples by molybdenum films to reduce friction and thermal gradients. Anyhow, samples underwent barreling after ausforming simulations.

A cylindrical specimen of size 10 × 4 mm was used for a pure dilatometry test, in which the sample was austenitized at 990 °C for 4 min and then cooled down to 300 °C fast enough so that no phases form during cooling. The temperature of 300 °C was held for 1 h before the sample was cooled down to room temperature. Also, three cylinders of size 10 × 5 mm were subjected to ausforming treatments. Those treatments started by an austenitization stage identical to the one that was previously described, after which samples were cooled down to the deformation temperature, T_{def} (520, 400 and 300 °C). After that, a temperature holding of 15 s took place before the compression step began. In that step, an engineering strain of 10% was applied, which promoted the formation of strain induced bainite when T_{def} = 400 °C and strain induced martensite when T_{def} = 300 °C, as confirmed in Ref. [6]. After the stress was removed, another temperature holding of 10 s was applied before cooling down to 300 °C, temperature which was held for 1 h. Finally, samples were cooled down to room temperature. The formation of fresh martensite was not detected by dilatometry during the final cooling of either of the thermal or thermomechanical treatments. The sketches of the treatments are included in Fig. 1(a) and further information on the parameters selection can be found in Ref. [8]. Table 1 includes some results obtained when characterizing these microstructures in the mentioned reference, such as the Vickers hardness (10 kg) HV10, the plate thickness measured on the transverse and longitudinal sections, t_T and t_L, respectively, and the austenite and ferrite volume fractions measured by X-Ray Diffraction, V_γ and V_α, respectively. These results are helpful to understand the subsequent research.

After treatments had finished, samples were cut longitudinally for further examination, using several techniques that will be subsequently described.

Firstly, a Struers Duramin-40-A2 versatile hardness tester was used to obtain Vickers hardness distributions along the longitudinal sections. To do so, samples were prepared by standard metallographic procedures. A load of 10 kg was applied with a step size of 0.6 mm. The analysis and representation of the data was performed by MatLab®.

Secondly, a JEOL JSM-6500 field emission gun scanning electron microscope (FEG-SEM) operating at 10 kV was used to characterize the microstructure in the two regions shown in Fig. 1(b). The characterization was aimed to be as close as possible to the Z-axis of the sample. The sample preparation for FEG-SEM included standard metallographic procedures and a final etching with a 2% nital solution.

Finally, samples were also scanned by EBSD by a SEM-FEG JEOL JSM-6500 operating at 15 kV. Two 79.68 × 60 μm^2 areas corresponding to the regions of interest were scanned on the longitudinal sections, using a step size of 0.16 μm. The sample preparation for EBSD also followed standard metallographic procedures, finally polishing with 50 nm colloidal silica suspension. The EBSD analysis was performed by means of the Matlab® toolbox MTEX [12].

The Student Edition of the commercial FE software ABAQUS/CAE (version 6.10), combined with Python scripting programming, was used to simulate the macroscopic state of stress and strain during compression tests at high temperature.

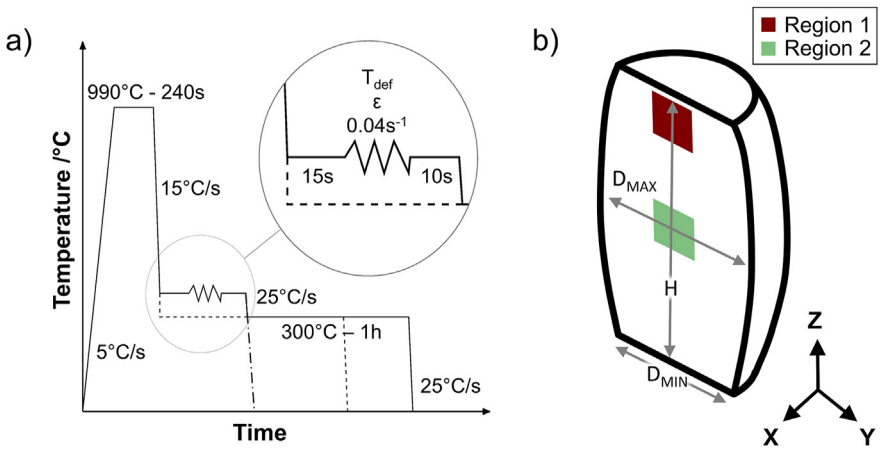

Fig. 1 – (a) Thermal and thermomechanical treatments performed in this work; (b) Sample subjected to hot compression, and thus undergoing barreling, where the regions that were microstructurally characterized are shown. Some critical parameters for the optimization of the Finite Element parameters are also described, i.e. D_{MAX}, D_{MIN} and H, see main body of the text for further details. T_{def} and ε stand for deformation temperature and applied engineering strain.

To simulate the stress and strain states during compression at a microscopic level, a Representative Volume Element (RVE) was generated by Dream.3D [13]. Later on, the compression state at the middle of one of the dilatometry specimens was performed following a full-field crystal plasticity approach by the spectral solver based on FFT (FastFourier Transform) provided by the software Damask [14].

3. Results

3.1. *Microstructural characterization*

Samples subjected to the thermal and thermomechanical treatments described in Section 2 were characterized.

Firstly, the samples hardness distributions were measured as described in Section 2, obtaining the results plot in Fig. 2(a-d). The rectangles surrounding the data aim to show the approximate dimension of the longitudinal section: 10 mm × 4 mm in Fig. 2(a) and 10 mm x 5 mm in Fig. 2(b-d). Note that the effect of barreling on these sections is not represented. Also, data corresponding to the same longitudinal distance were averaged to study how hardness varies from the sample top surface to the sample center. Results can be found in Fig. 2(e), where the error bars correspond to the standard deviations. It can be seen that: a) the hardness is homogeneous along the longitudinal section for the sample isothermally treated; b) hardness variations are detected along the sections of the ausformed samples, although different trends are found. Whereas hardness decreases as approaching the sample centers of the samples ausformed at 520 and 400 °C, a maximum hardness is detected in the center of the sample deformed at 300 °C; c) the trend of the HV10 values in the sample center are the same than the ones included in Table 1.

Table 1 – Results obtained when characterizing the same microstructures of this work in the central part of the specimens, as reported in Ref. [8], where HV10 stands for Vickers hardness (10 kg), t_T and t_L mean plate thickness measured on the transverse and longitudinal sections, respectively, and V_γ and V_α are the austenite and ferrite volume fractions.

Condition	HV10	t_T/nm	t_L/nm	V_γ/%	V_α/%
Isothermal	562 ± 2	53 ± 3	52 ± 1	15 ± 3	85 ± 3
T_{def} = 520 °C	569 ± 3	56 ± 2	56 ± 2	21 ± 3	79 ± 3
T_{def} = 400 °C	530 ± 9	56 ± 3	46 ± 2	24 ± 3	76 ± 3
T_{def} = 300 °C	581 ± 4	53 ± 2	46 ± 1	26 ± 3	74 ± 3

The hardness differences detected suggested that there was a microstructural gradient along the samples. Hence, two different regions were selected to be characterized: one area by the top surface on the longitudinal section and one area in the center of the longitudinal section. Those areas are named Region 1 and Region 2 from now on, see Fig. 1(b). These areas were examined by FEG-SEM, and representative examples of the microstructures in the corresponding regions for all tested conditions can be seen in Fig. 3. All microstructures are bainitic, as previously pointed out in Section 2, so the microstructures are constituted by bainitic ferrite plates and highly carbon enriched retained austenite. Whereas microstructures obtained for the isothermal condition in Region 1 and Region 2 are apparently similar in terms of the distribution of the plates and scale, see Fig. 3(a,b), some differences are found when comparing microstructures in those two regions for the ausforming conditions. In terms of the bainitic ferrite plates distributions, it can be observed that plates are aligned within prior austenite grains in Regions 2, especially for the ausforming treatments with T_{def} = 400 °C and 300 °C (Fig. 3(f,h)). However, in Regions 1, that alignment is only slightly evident for the ausforming treatments at 300 °C, see Fig. 3(g). If one compares Fig. 3(c,e,g) to Fig. 3(d,f,h), it can be seen that plates are apparently coarser in Regions 1, where the thickness of the bainitic ferrite plates seems much less homogeneous. This may be due to the fact that some bainitic ferrite plates found

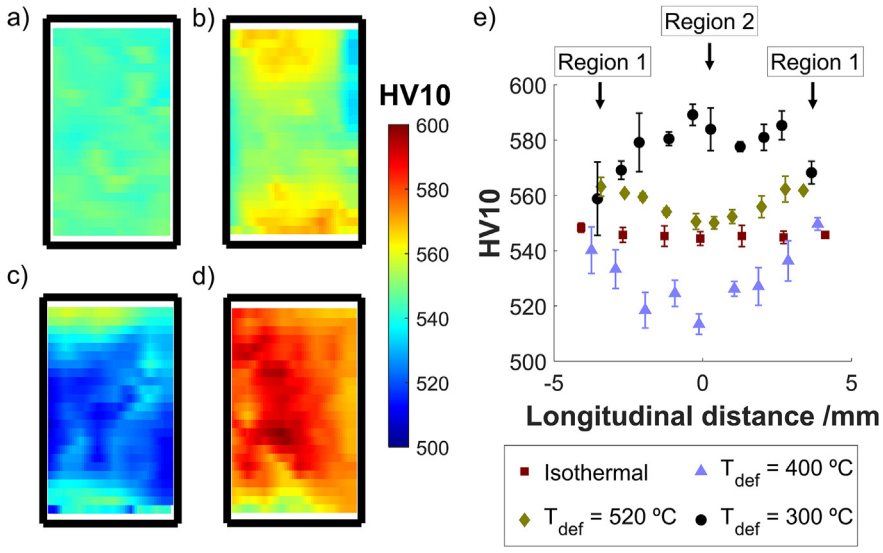

Fig. 2 – (a–d) HV10 distributions for samples subjected to: (a) pure isothermal treatment; (b) ausforming treatment with T_{def} = 520 °C; (c) ausforming treatment with T_{def} = 400 °C; (d) ausforming treatment with T_{def} = 300 °C; (e) averaged HV10 values along the vertical direction for all four mentioned conditions. The error bars correspond to the standard deviation.

especially in Regions 1 seem to have merged, i.e. some coalescence bainite is observed, such as the one shown in the high magnification images in Fig. 3(c,e,g).

Finally, EBSD measurements were carried out in Regions 1 and 2 for all tested conditions. Fig. 4 shows the scanned EBSD maps showing the orientations of the bcc phase, where the coloring corresponds to the Z-axis Inverse Pole Figure (IPF) that can be seen in the right bottom of the image. The black lines delimit areas with similar orientation – blocks – where the considered threshold angle was 10°. The EBSD maps were used to quantify variant selection at Regions 1 and 2. To do so, the methodology explained in Ref. [11] was applied. This methodology consists of the reconstruction of the prior austenite and the determination of the OR by the software developed by Nyyssönen et al. [15] and the determination of the variant number corresponding to each bcc block. Subsequently, the area percentage of every variant belonging to its corresponding prior austenite grain (PAG) has to be determined. A PAG which is not governed by any variant selection effect should ideally have 24 variants, each with the same area percentage, i.e. 4.2%. In each PAG j, the n variants whose area percentage exceed 4.2% were named predominant variants. The area percentage of the most predominant variant in a PAG j was called $AP_{V-max,j}$. The nomenclature was kept from Ref. [11]. A sample with strong variant selection should present a small average n, i.e. there are few variants that are predominant, accompanied by an increase of the average area of any predominant variant. Fig. 5 shows the box-plots representing the relative frequency of n (Fig. 5(a)) and the relative frequency of $AP_{V-max,j}$ (Fig. 5(b)). In the boxplots, the boxes are delimited by the lower and upper quartiles (Q_1 and Q_3, respectively) and the lines crossing through them are the median, Q_2. The whiskers start at the lowest datum within 1.5 times IQR (IQR = Q_3- Q_1) below Q_1 and finish at the highest datum within 1.5 times IQR above Q_3. The outliers are represented by triangles and the mean values are represented by squares. As can be observed, as T_{def} is decreased down to T_{def} = 400 °C, histograms in Fig. 5(a) corresponding to the same region move down, as there are fewer variants in every PAG, and histograms in Fig. 5(b) move up, as the most predominant variant takes more area percentage in every PAG. The effect is reversed for T_{def} = 300 °C, which seems to have a less pronounced variant selection in comparison with the condition T_{def} = 400 °C, opposite to the data reported in Ref. [11]. In any case, it seems that variant selection is stronger in Regions 2 than in Regions 1, being this effect more pronounced for the two lowest T_{def}.

3.2. *Finite elements analysis*

The macroscopic states of stress and strain during dilatometer hot compression tests were simulated by using ABAQUS/CAE, combined with Python scripting. The model consisted of two punchers and a cylinder, as can be observed in Fig. 6, where a friction existed in between both punchers and the cylinder (μ).

The punchers were modelled as analytical rigid parts because the compression punchers that the dilatometer uses to deform the samples are made of Si_3N_4, whose strength is very high (3 GPa [16]). The dimensions of the punchers are not relevant.

The cylindrical dilatometry sample, of height H_0 (= 10 mm) and diameter D_0 (= 5 mm), was modelled as a deformable part, composed of 952 nodes, 728C3D8R elements and made of an elastoplastic material, whose input parameters were the Young Modulus (E), the Poisson ratio (ν), and the true stress-true plastic strain curve.

The simulation consisted of two steps: loading and unloading. During loading, the bottom puncher was fixed and the upper one was made to move down a distance along the Z-axis (Δz), towards to sample. The modification of the loading

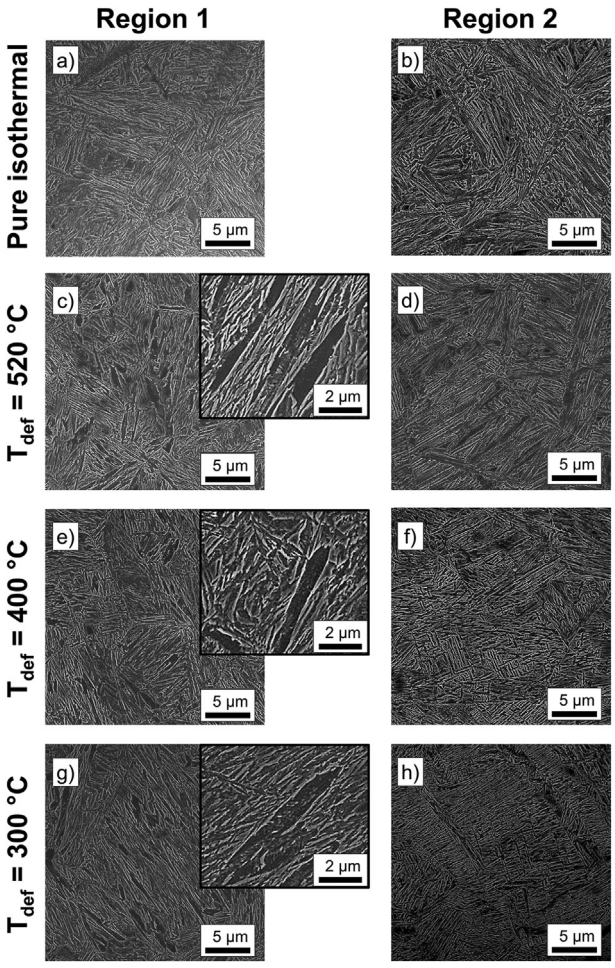

Fig. 3 – Microstructures obtained by different thermal and thermomechanical treatments: (a–b) pure isothermal treatment; (c–d) ausforming treatment with T_{def} = 520 °C; (e–f) ausforming treatment with T_{def} = 400 °C; (h–i) ausforming treatment with T_{def} = 300 °C. Whereas subfigures (a,c,e,h) correspond to Region 1 in Fig. 1 (including a higher magnification image where coalescence bainite is shown for the ausforming conditions), subfigures (b,d,f,i) correspond to Region 2 in the same figure.

time (t) enables to set the strain rate $\dot{\varepsilon}_p$. The true stress tensors of the elements which are on the upper cylinder surface and the height of the sample were recorded throughout the whole loading step to later construct the output true stress-true strain curve. The unloading step consisted in moving backwards the upper puncher to let the sample elastically relax. After unloading, the sample would be of height H. Note that $\Delta z \neq H_0 - H$ because sample dimensions also change because of the elastic relaxation. In addition, the sample would have undergone barreling because of the friction with the punchers, so it would be characterized by a maximum diameter (D_{MAX}, found at half height) and a minimum diameter (D_{MIN}, found at the upper and bottom surfaces of the sample), see Fig. 1(b). Note that both D_{MAX} and D_{MIN} are larger than the initial diameter D_0.

Regarding the units used for the simulation, although it is known that ABAQUS runs without units, it is important that the input parameters units are consistent. In this work, the SI (mm) system of units was used, please refer to the ABAQUS online documentation [17] to find the units corresponding to each parameter.

The simulation required several input parameters, which were calibrated as explained in Appendix A. After calibration, the compression steps of the ausforming treatments described in the previous section were simulated. Fig. 7 shows the Von Mises (VM) stress distributions of the three samples, before and after unloading, in addition to the Equivalent Plastic Strain (EPS) distributions. It can be observed that all distributions show the typical X-shaped distributions reported in previous works and characteristic of a triaxial state [18,19], where the central part of the sample is the one that is subjected to the highest VM stress during the loading step (Fig. 7(a-c)), being thus the most plastically deformed (Fig. 7(g-i)), although after unloading its VM residual stresses are the lowest (Fig. 7(d-f)). The opposite scenario is found for the regions close to either the top or the bottom surfaces, where lower VM stresses and EPS are detected during the deformation step, but the residual VM stress is higher after unloading.

To better understand the state of stress and strain in the regions of interest characterized in the previous section, the evolution of the diagonal components of stress and plastic strain with simulation time in Region 1 and 2 for each of the simulations can be found in Fig. 8. The location of the nodes from which such tensors were taken can be found in Fig. 7, represented by black squares (Region 1) and triangles (Region 2). Note that, even though it was tried to select the nodes so that they were as close as possible to the Z-axis, they are still slightly apart from it (approx. 0.6 mm) because of the restrictions of the mesh. Although this distance is rather high in comparison to the size of the SEM or EBSD images, the shear stresses or shear plastic strains - according to the XYZ coordinate system - are still low (below 5 MPa or 0.01) – note that these components would be expected to be zero if nodes were right on the Z-axis. Thus, these shear components are not shown in Fig. 8 and it can be assumed that the X, Y and Z axes are the principal axes, i.e. the diagonal components are the principal components.

As can be observed, the behavior is rather similar regardless of $T_{def.}$, although the stress levels slightly increase as T_{def} is lower. The stress tensor is different in Regions 1 than in Regions 2: whereas Regions 2 are practically undergoing uniaxial compression during the whole loading step, being their radial ($Stress_{XX}$ and $Stress_{YY}$) principal stress components never higher than 5 MPa, Regions 1 show a triaxial state, where the radial principal stress components can go down to almost −60 MPa and the longitudinal principal stress component ($Stress_{ZZ}$) can go down to −490 MPa. Note that the VM stresses, which were shown to be lower in Regions 1 during loading, depend on the difference between the principal components of the stress tensor. For that reason, even though Regions 1 reach a more negative longitudinal principal stress, the negative values of $Stress_{XX}$ and $Stress_{YY}$ compensate and makes the VM stress lower. Regarding the residual stresses (grey shadowed regions in Fig. 8), whereas none of the principal components of the stress tensors in Regions 2 are

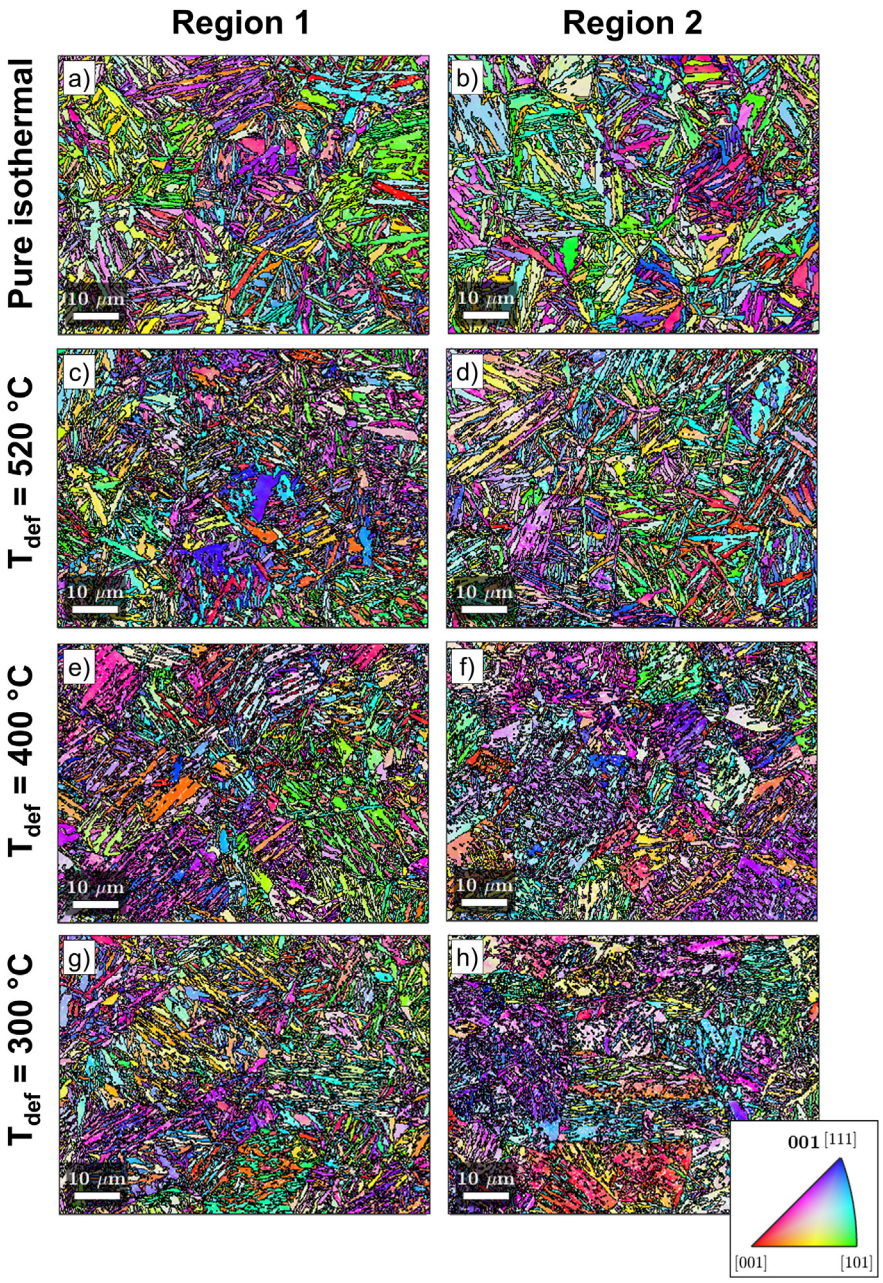

Fig. 4 – EBSD maps showing the orientations of the bcc phase, where the coloring corresponds to the Z-axis Inverse Pole Figure that can be seen in the right bottom of the image. The black lines delimit areas with similar orientation – blocks – where the considered threshold angle was 10°.

above 6 MPa in absolute value, the longitudinal principal component of the stress tensors in Regions 1 can go down to −30 MPa, being the radial components below −10 MPa. These results are in good agreement with a lower VM residual stress in Regions 1.

3.3. *Crystal plasticity*

To further study the role of plastic deformation on variant selection, the compression state at the middle of one of the dilatometry specimens (Region 2, $T_{def} = 400\,^{\circ}C$) was performed following a full-field crystal plasticity approach by the spectral solver based on FFT (FastFourier Transform) provided by the software DAMASK [14]. The mentioned condition was selected as variant selection is pronounced in that case. A complete description of the constitutive equations used for the elastic and plastic deformation of synthetic microstructures can be found in Ref. [14]. The explanation of the constitutive hardening equations used for this simulation and the calibration of the model can be found in Appendix B.

A synthetic microstructure of dimensions 60 × 60 × 100 voxels^3 (1 μm/voxel) was generated for DAMAK simulations by the Dream 3D software [13]. Although this microstructure is representative of the austenite microstructure statistics in terms of grain size distribution – shown in Fig. 9(a) [8] - it only has 62 grains so that the mesh can be fine enough to

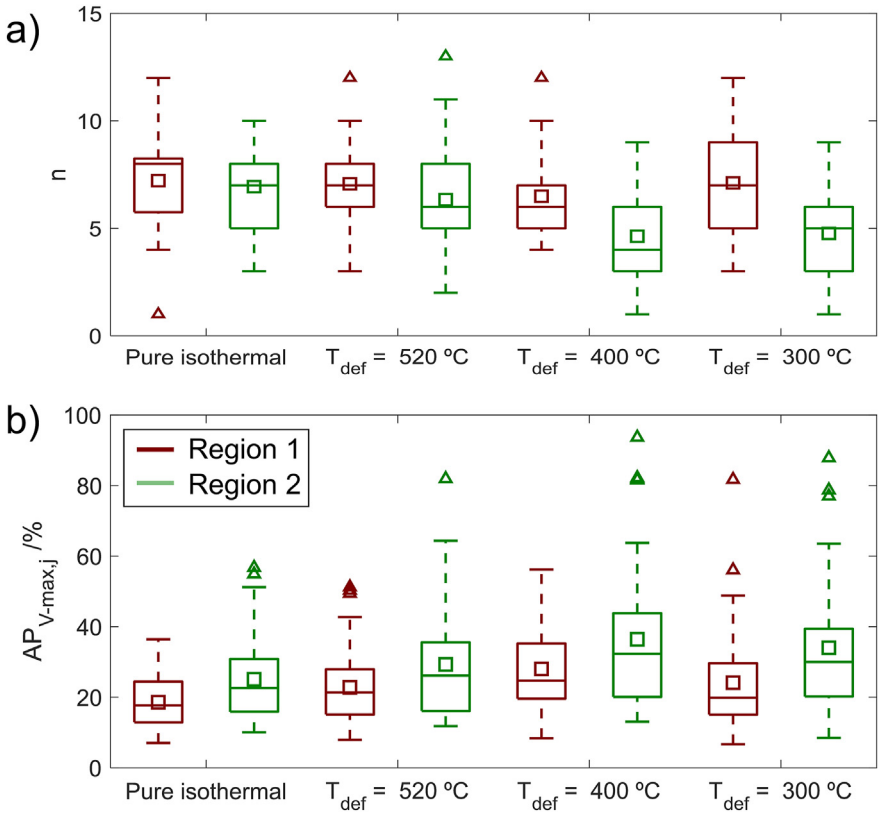

Fig. 5 – Boxplots representing (a) the relative frequency of n – number of predominant variants -; (b) the relative frequency of the area of the most predominant variant $AP_{V-max,j}$. Refer to Ref. [11] for a more detailed definition of those variables. Boxplots are colored according to the region they belong to. In the boxplots, the boxes are delimited by the lower and upper quartiles (Q_1 and Q_3, respectively) and the lines crossing through them are the median, Q_2. The whiskers start at the lowest datum within 1.5 times IQR (IQR = Q_3- Q_1) below Q_1 and finish at the highest datum within 1.5 times IQR above Q_3. The outliers are represented by triangles and the mean values are represented by squares.

have good resolution, while keeping the computing time low. The RVE texture was initially representative of the one of the prior austenite texture (before deformation takes place) measured by XRD texture measurements [11], see Fig. 9(b). However, the orientation of 13 grains of the RVE, all of them contained in the middle YZ section of the RVE, were modified to mimic the orientations of the EBSD map taken for that condition (Region 2, T_{def} = 400 °C) and presenting strong variant selection in a prior austenite grain. Fig. 10(a, b) show the cropped bainitic ferrite and reconstructed austenite IPF EBSD maps corresponding to the mentioned condition, where the bainitic ferrite grown in the biggest green prior austenite grain on the center of Fig. 10(b) presented a pronounced variant selection. As can be observed, in that prior austenite grain, bainitic ferrite plates grew at about ±45° with respect to the compression direction (vertical). Thus, in this analysis, the attention is particularly payed to that grain. Fig. 10(c) shows the modelled YZ section with IPF coloring, where it can be observed that the orientation of the grain of study and the surrounding grains corresponds to the orientations in Fig. 10(b). Note that it was assumed that the experimental Euler orientations had not changed significantly with the small deformation that had been applied. Fig. 10(d) shows the orientations (IPF coloring) of the same grains after simulating its compressive (vertical) deformation, where it can be confirmed that the orientations do not vary significantly, and the assumption was correctly made.

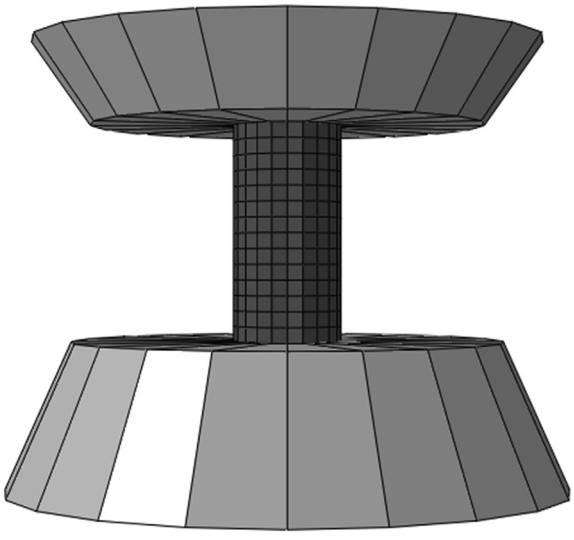

Fig. 6 – FE model for dilatometer hot compression test before applying any deformation. The initial dimensions of the cylinder were H_0 = 10 mm and D_0 = 5 mm.

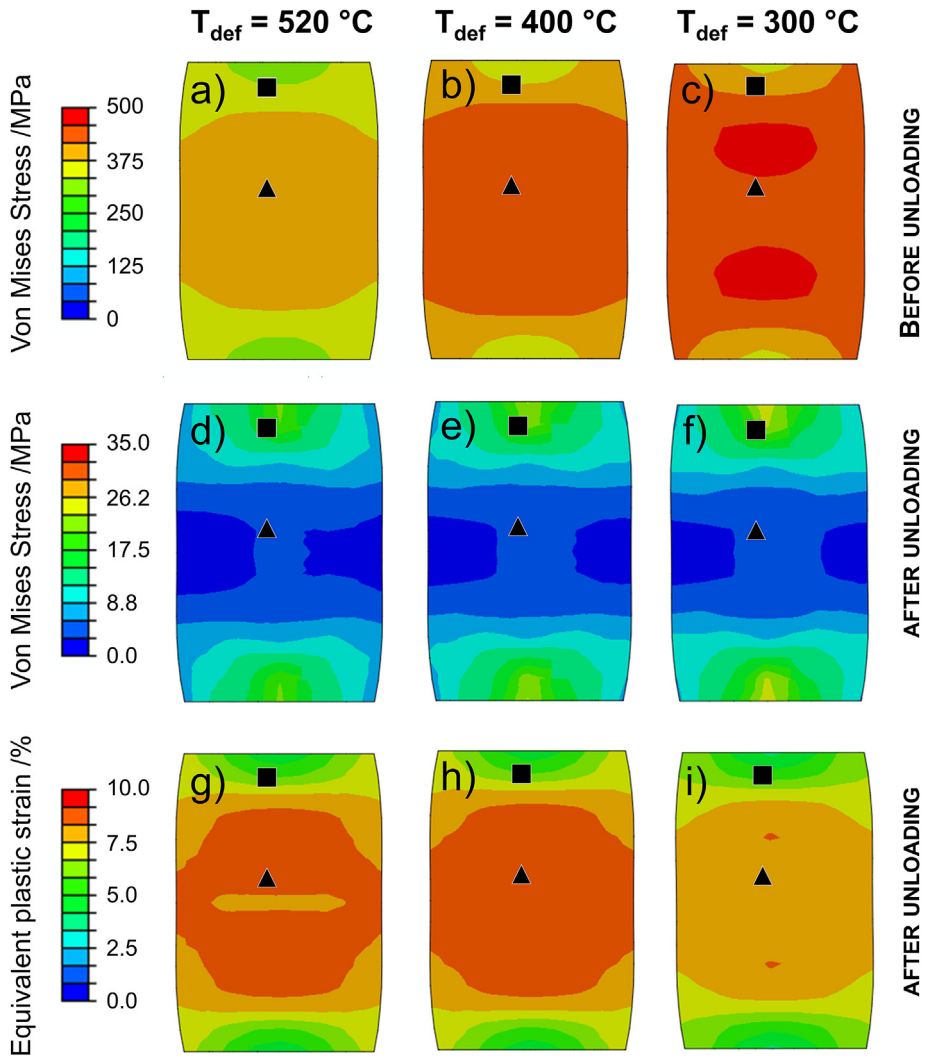

Fig. 7 – (a–c) Von Mises Stress distributions of samples before unloading; (d–f) Von Mises Stress distributions of samples after unloading; (g–i) Equivalent plastic strain of samples after unloading. The input parameters were varied so that sample properties correspond to the T_{def} shown on the top part of the figure. The black squares and triangles show the location of the nodes from which the stress and plastic strain tensors were extracted.

Fig. 10(e,f) shows the VM stress and VM strain distributions of the same section after deformation. The most interesting distribution of these two is the second one, as it can be observed that the VM strain in the grain of study is not homogeneous, but it is distributed along microbands which lay at about 45° with respect to the compression direction, approximately parallel to the traces of the habit planes of the grown bainitic ferrite plates in Fig. 10(a).

4. Discussion

Firstly, it is important to point out that the characterization of the sample subjected to the isothermal treatment already enables to confirm that the temperature gradient during the isothermal treatment in the dilatometer was negligible, as the hardness does not vary along the sample in that case, see Fig. 2(a, e), which is in good agreement with the fact that micrographs in Fig. 3(a) and (b) do not present apparent differences. This is an important datum as it rules out the possibility of a temperature gradient affecting the phase transformations happening in the treated samples and thus being responsible of the microstructural heterogeneity in the sample. The differences among the transformations happening in Regions 1 and 2 that are discussed subsequently for the ausforming samples can only be due to the different stress or strain states in both regions. No residual stresses due to the difference of temperature along the samples are expected either: it can be assumed that the state of stress and strain after unloading is the same than the state of stress and strain before bainitic transformation takes place – note that, a temperature gradient in the sample would affect the states of stress and strain while cooling the samples down. Hence, the present simulations, combined with the characterization can help to understand the phase transformations and their driving mechanisms in the studied samples.

To understand the characterization performed in Section 3.1. based on these simulations, one must also consider that,

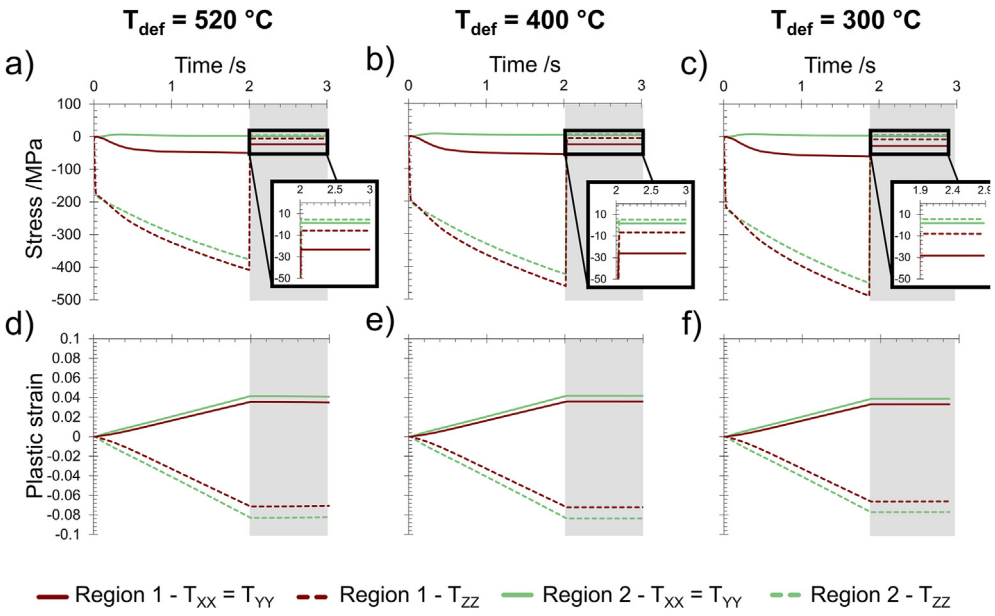

Fig. 8 – Evolution of the principal components of stress and plastic strain with simulation time in nodes representative of Region 1 and Region 2 for each of the simulations. The white areas represent the loading step, whereas the unloading step is depicted by a shadowed area. The detail in subfigures a-c corresponds to the unloading step.

in a previous study [6], it was shown that the samples deformed at 400 °C and 300 °C underwent bainite and martensite strain induced transformations, respectively, at least in Regions 2. The FE simulations pointed out the fact that Regions 2 are subjected to higher VM stresses during the loading step than Regions 1, where the stresses are close to uniaxial in the former case and they are triaxial in the latter one. Also, the EPS take their highest value in Regions 2. Displacive strain induced transformations are more promoted as the stress is higher [20], which means that the amount of strain induced bainitic ferrite/martensite formed in Regions 2 is expected to be higher than the amount of strain induced bainitic ferrite/martensite formed in Regions 1.

Once this is known, the hardness results can be discussed. First, the hardness variations detected along the sections of the sample deformed at 520 °C in Fig. 2(e) can be explained if one assumes that the amount of retained austenite is higher in Regions 2 (sample center) than in Regions 1 (by the surface). The increase of the fraction of retained austenite is due to the mechanical stabilization of austenite, which is more pronounced where the EPS is higher (Regions 2) [3,4,21]. Anyhow, the hardness values are always higher than the ones reported for the pure isothermal treatment, even though the bainitic ferrite plate thickness is similar and the retained austenite volume fraction is higher in the ausformed condition than in the isothermal one - at least in Regions 2, see Table 1 –. This may be due to the increased strength of the ferritic matrix and the retained austenite [8]. In the sample deformed at 400 °C, the trend is the same, although the hardness values are the lowest ones among all the studied samples. This behavior can be explained by the formation of strain induced bainite during the deformation step. The strain induced bainite is coarser, because it was formed at higher temperatures (400 °C) than the isothermal temperature (300 °C), note that it is known that the plate thickness decreases with the transformation temperature [22]. The presence of coarse strain induced bainite affects the mean plate thickness, which is lower in comparison with the one reported for the condition ausformed at T_{def} = 520 °C, as shown in Table 1. As previously mentioned, displacive strain induced transformations are more promoted as the stress is higher [20], which suggest that the highest amount of strain induced bainite can be found in Region 2, where the HV10 is lowest. The HV10 values of the sample deformed at 300 °C present a convex profile, opposite trend to the one in the last two mentioned samples, which is due to the formation of strain induced martensite during the deformation step. The fraction of strain induced martensite is higher in Region 2 than in Region 1, as the VM stress is higher there. This strain induced martensite was the major contributor to the hardness increase.

The coalescence of bainitic ferrite plates can also be discussed. As previously mentioned, this phenomenon is apparently more pronounced in Regions 1 than in Regions 2. The coalescence of bainitic ferrite plates can be affected by the residual stress states in these regions. The FE simulation showed that, whereas none of the principal components of the residual stress tensors in Regions 2 are above 6 MPa in absolute value, the longitudinal principal component of the stress tensors in Regions 1 can go down to −30 MPa, being the radial components below −10 MPa. In previous works [23,24], it has been reported that the application of a tensile stress can promote the coalescence of bainitic ferrite plates. However, the effect of uniaxial compression stresses or the effect of triaxial stresses, as the ones reported for Regions 1, has not been yet discussed. The presence of a residual compressive stress could have the same impact at the microscopic level

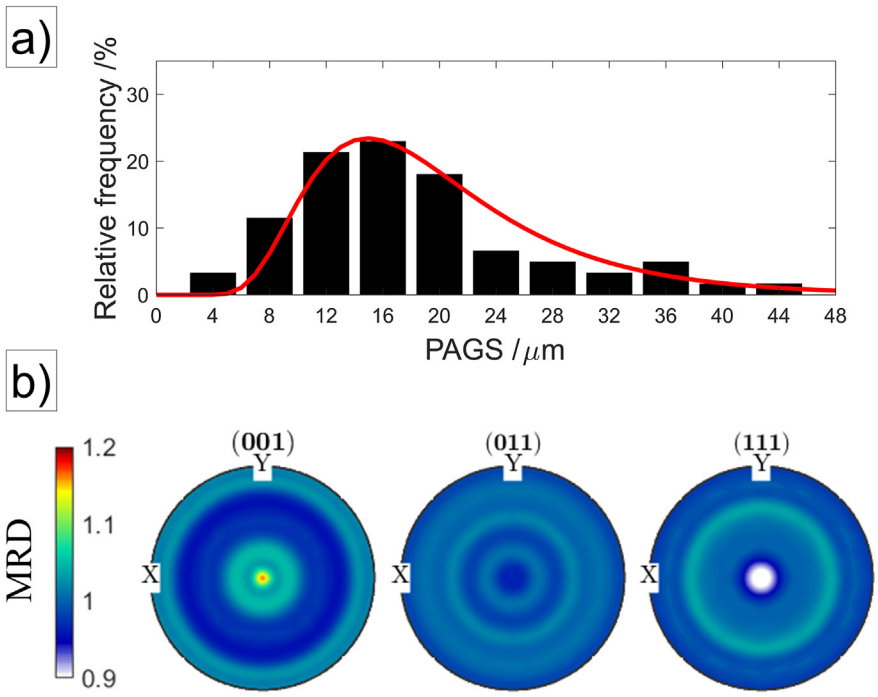

Fig. 9 – (a) Histogram showing the prior austenite grain size measured in Ref. [8], where the red line represents the lognormal distribution which was input for the crystal plasticity simulation; (b) Pole figures showing the texture of the retained austenite of the isothermally treated sample, texture which was shown to be equal to the prior austenite texture (before deformation takes place) in Ref. [11]. MRD stands for multiples of random distribution.

than the application of an external load. Therefore, the residual stresses found in Regions 1 could have promoted the coalescence of bainitic ferrite plates in Regions 1.

Finally, the results given by the FE simulation can also help to make conclusions on the effect of the residual stress and the plastic strain on the selection of crystallographic variants during ausforming treatments. Please, note that the effect of the strain induced transformations on variant selection can be neglected for these treatments, as it has been reported that the trends observed in these same microstructures (same treatments) in terms of variant selection are not modified by the presence of strain induced phases [11]. Results in Section 3.1. showed that variant selection is stronger in Regions 2, where the EPS is higher and the VM residual stress is lower, than in Regions 1. These results evidence that the effect of the residual macroscopic stresses on the observed variant selection is negligible, as stronger variant selection is found in the regions where the residual stresses are lower, in good agreement with previous works [19,25], and that it is plastic deformation which plays a role in variant selection, as proposed elsewhere [7,26–30].

The crystal plasticity simulation can help to better understand the interaction between the plastic deformation and the selection of crystallographic variants. As mentioned, in Section 3.3. the deformation seems to be distributed along deformation microbands which lay at about ±45°, parallel to the traces of the habit planes of the grown bainitic ferrite plates. This results are in good agreement with previous works in which ausformed lath martensite was shown to grow along deformation microbands (their habit plane was parallel to the slip plane) [28,31,32]. Miyamoto et al. [32] stated that the ausformed martensite preferentially nucleated on microband structures as a result of a smaller amount of activation energy and, also, its growth across microband boundaries was inhibited. Miyamoto et al. reported a similar profile fraction of variant vs. variant number than for the treatments of study, reported in Ref. [11], where variants belonging to the first and the third crystallographic packets were more prone to form. They also showed that the variant selection phenomenon was more pronounced in prior austenite grains whose <0 1 1> direction was parallel or close to parallel the deformation direction. Please note that the typical fcc compression texture is characterized by having the <0 1 1> direction parallel to the compression direction. This texture is the one found in bainitic ferrite for all the ausformed conditions [11], presenting the sample deformed at the lowest temperatures the strongest texture. Interestingly enough, the <0 1 1> direction of the grain of study in Fig. 10 (grain which showed the most pronounced variant selection among its neighbors) is close to be parallel to the compression direction. These results suggest that the mechanism described for ausformed lath martensite by Miyamoto et al. [32] can be also applied to the ausformed bainite in this study.

5. Conclusion

The main conclusion of this work is that the variant selection shown in ausformed bainitic microstructures can be

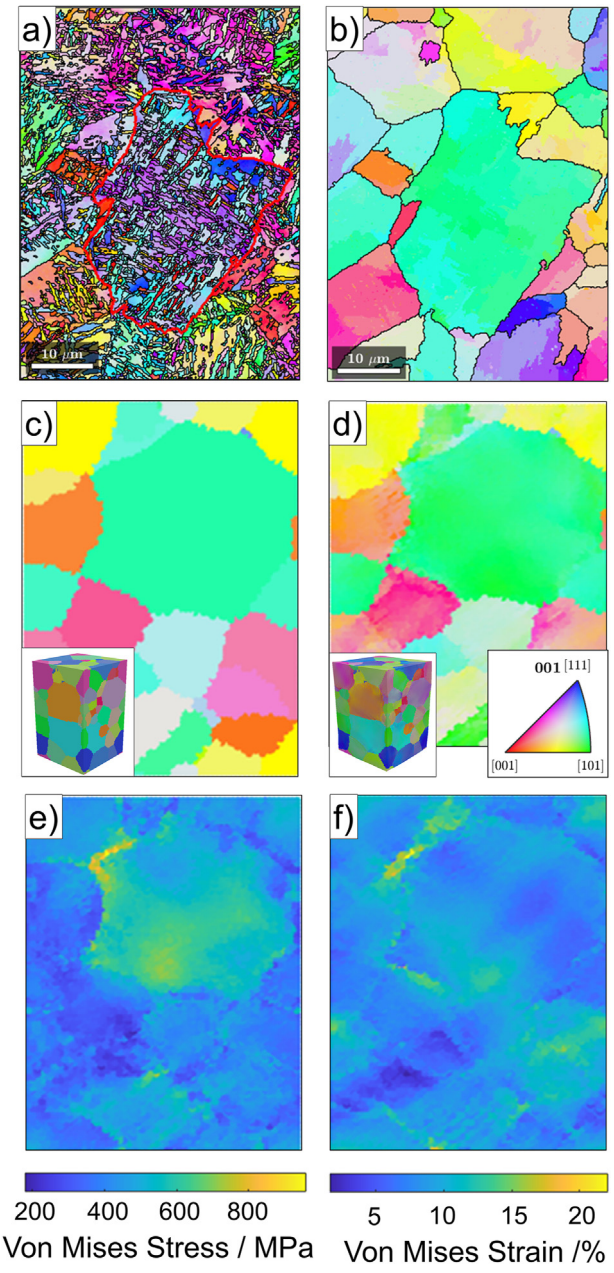

Fig. 10 – (a) Cropped bainitic ferrite Inverse Pole Figure (IPF) EBSD map corresponding to Region 2, $T_{def} = 400$ °C; (b) Cropped reconstructed austenite Inverse Pole Figure (IPF) EBSD map corresponding to Region 2, $T_{def} = 400$ °C which was mimicked to be simulated by Damask; (c) middle YZ section of the initial (pre-deformation) RVE, to be compared with subfigure (b) and (on the left bottom) whole initial (pre-deformation) RVE, with IPF coloring; (d) middle YZ section of the final (post-deformation) RVE and (on the left bottom) whole final (post-deformation) RVE, with IPF coloring, where the legend is on the right bottom; (e) Von Mises Stress distribution in the middle YZ section of the RVE; (f) Von Mises Strain distribution in the middle YZ section of the RVE. The compression direction is always vertical.

explained by understanding the distribution of the plastic strains at the macro and micro level. The selection of crystallographic variants is more pronounced in the regions which have been more deformed (and which present lower residual stresses). Also, the carried out crystal plasticity simulation has evidenced that the deformation distributes along deformation microbands, along which the most promoted variants seem to grow, in good agreement with results reported by Miyamoto et al. [32] in ausformed lath martensite.

Funding

This work was supported by the European Research Fund for Coal and Steel under the Contract RFCS-2019-899482 and the German Research Foundation (DFG) under the project 411091845.

Declaration of Competing Interest

The authors declare that they have no known competing financial interests or personal relationships that could have appeared to influence the work reported in this paper.

Acknowledgments

We acknowledge the support of the Technical University of Madrid for the license of the software Abaqus Student Edition. We would also like to thank José Prada Casas (Struers), who helped the authors to calibrate and use the Duramin-40-A2 versatile hardness tester.

Appendix A. Calibration of the FE simulation

The FE simulation required several input parameters, such as the Young Modulus (E), the Poisson ratio (ν), the true stress-true plastic strain curve, the friction coefficient between the sample and the dilatometer punchers (μ), the distance that the upper puncher moved during the loading step (Δz) and the loading time (t).

A dilatometer hot compression test, followed by a quenching step, was performed as a reference to optimize the simulation parameters. The scheme of the mentioned treatment is depicted by a dash-dotted line in Fig. 1(a), where T_{def} and ε were decided to be 520 °C and 30%, respectively, as strain induced transformations have shown not to modify the stress–strain curve at this temperature up to such strain in the same steel of this work [6].

The value of ν was unknown and it was assumed to be 0.3, similar to the value reported in the literature for austenitic steels at similar temperatures [33]. Regarding the value of E, the experience of the authors with this equipment is that the elastic deformation of these punchers cannot be avoided, making impossible to estimate the elastic properties of the material of study. For that reason, the elastic part was always

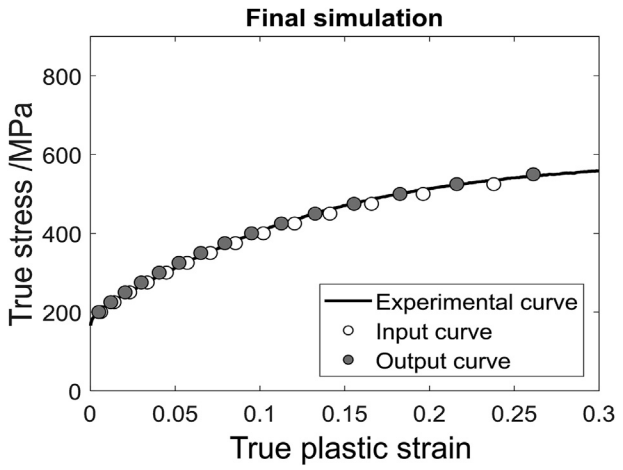

Fig. A1 – Final input and output true stress-true strain curves obtained after optimizing the simulation parameters, compared to the experimental true stress-true strain curve.

subtracted from any stress–strain curve before any comparison is made and E could not be estimated from experimental results. Hence, E was assumed to be 200 GPa, similar value to the ones reported for austenitic steels at similar temperatures [33,34]. The values of Δz and t must vary depending on the required value of the final height H and the strain rate $\dot{\varepsilon}_p$, respectively. The loading time was always calculated as $t = \Delta z/\dot{\varepsilon}_p$, where $\dot{\varepsilon}_p = 0.4$ mm/s in this work.

Regarding the friction coefficient μ, it principally alters the sample dimensions (H, D_{MAX}.and D_{MIN}, see Fig. 1(b)) by the barreling effect. The experimental initial height and diameter (H_0 and D_0) were measured before the mentioned experimental test started and H, D_{MAX}.and D_{MIN} were measured after the test was finished. The values of the mentioned values can be found in Table A1. The dimension changes associated to cooling the sample down (negative change in length) and to the martensitic transformation (positive change in length) undergone during cooling were assumed to be negligible; note that the change in length associated to cooling the same steel of this study down from 520 °C, after full austenitization, to room temperature has been reported to be about 20 μm [8].

In addition, the input true stress – true plastic strain had to be optimized so that the simulated compression behavior was as similar as possible to the one obtained by the dilatometer, as it has been reported that barreling can alter the compression curves so that they are not the same than the ones that would be obtained for an uniaxial test (with $\mu = 0$) [18]. To simplify the variation of the input true stress-true strain curve, it was decided to use the Johnson and Cook (JC) model to define the engineering stress-plastic strain curve, taking advantage of the fact that such curve had already been fitted for the same steel and at the same temperature in a previous work [6] and, therefore, such parameters could be used as initial ones for the optimization. The JC model reads as follows:

$$\sigma = \left(A + B\varepsilon_p^n\right) \cdot \left(1 + C\ln\left(\frac{\dot{\varepsilon}_p}{\dot{\varepsilon}_{p0}}\right)\right) \cdot \left(1 - \left(\frac{T_{def} - T_r}{T_m - T_r}\right)^m\right) \quad \text{(A1)}$$

where σ is the stress, $\dot{\varepsilon}_{p0}$ is the reference strain rate (which was equaled to the experimental strain rate $\dot{\varepsilon}_p$ not to have to fit C), T_r and T_m are the room and the melting temperatures and A, B, C, n and m are constants that must be fitted for every steel. However, because the parameter m describes the influence of T_{def} on stress and the simulation is only compared to data corresponding to one temperature (520 °C), it was decided to keep m fixed (equal to the experimental value: m = 1.0). The values of T_r and T_m were assumed to be 25 and 1497 °C, respectively. Further information on the JC model and the meaning of its parameters can be found in Ref. [6]. Note that, to be input in ABAQUS, the engineering curve given by the JC must be converted to the true one.

To optimize the mentioned parameters, Python scripting was used in combination with ABAQUS. Using Python scripting enables to automatically modify the model parameters, run the simulation and post-process the results given by the simulation as desired, among others [17]. The error was defined as the summation of the relative error between the experimental and the simulated true stress-true strain curve, H, D_{MAX} and D_{MIN}. This error was minimized by a simple function written by the authors, which consisted in varying the input parameters, starting from some initial values decided by the user, until the error was minimal. The initial parameters of the JC model, in addition to the initial values taken for μ and Δz are included in Table A2.

The optimized parameters obtained after running the minimization function are included in Table A2. As can be observed in Fig. A1, the output true stress-true strain curve perfectly fits the experimental one. Note that the alteration of the stress–strain curve is not significant in this case as the barreling effect is not too pronounced, whereas barreling in Ref. [18] was much more evident. Regarding the sample dimensions, the comparison between the experiment and the simulation in terms of H, D_{MAX} and D_{MIN} can be found in Table A1, where it can be observed that the error is low in every case, only in the case of D_{MAX} the error is higher than 1%. This means that the FE method was not able to correctly simulate the barreling effect, even though D_{MIN} is similar to the experimental, which could be a result of not considering the heat transfer during compression, as has been considered in other works [18]. Although this could alter the calculation of the stress and strain along the sample, we assume that the alteration is not high and that the distributions do not vary significantly.

Table A1 – Initial and final dimensions of the experimental compression samples and the simulation compression part used for the optimization of the simulation parameters.

Parameter	Experimental/ mm	Simulation/ mm	Simulation relative error/ %
H_0	10.0	10.0	0.1
D_0	5.0	5.0	0.2
H	7.3	7.3	0.0
D_{MAX}	6.0	5.8	4.1
D_{MIN}	5.4	5.4	0.1

Table A2 – Initial values of the parameters input in the minimization function and optimized values of the same parameters.

	A/MPa	B/MPa	n	μ	Δz/mm
Initial	282	3407	0.89	0.09	2.70
Final	265	3000	0.84	0.14	2.72

For simulating the stress and strain state at other the deformation temperatures used in this work, all the parameters were kept constant, except the true stress – true plastic strain curve, which was very easily modified, as the JC model includes the effect of the temperature. We assume that the variation of the left parameters with low variation of deformation temperature (max. 220 °C) is not very pronounced. As the ausformed samples studied in this work were only deformed up to lower values than the one used for the calibration (the values of H after the ausforming treatments at 520, 400 and 300 °C were 9.2, 9.2 and 9.3 mm, respectively), the values of Δz were changed for every simulation so that the simulated cylinder H was the same than the experimental H after performing the corresponding ausforming treatments, assuming that the changes in length because of cooling and bainitic transformation are negligible. To reach such values, Δz of 0.8 mm were applied in all cases. The loading time t was modified consequently.

Appendix B. Calibration of the crystal plasticity simulation

Here, only the constitutive hardening equations are presented and their suitability for the current study discussed. The hardening of austenite is assumed to occur only by slip and other effects such as twinning or mechanical induced martensite transformation, which might play a role in the deformation process of the austenite in the present material and conditions, are obviated for sake of simplicity. Hence, the widely adopted phenomenological power law is used for the description of slip hardening, see Equation (B1).

$$\dot{\tau}_C^{\beta} = \sum_{\eta} h_{\beta\eta}\dot{\gamma}^{\eta} \tag{B1}$$

The evolution of critical shear stress in the slip plane β, is given by its time derivative $\dot{\tau}_C^{\beta}$. The instantaneous slip-system hardening moduli $h_{\beta\eta}$, in general, depends on the history of slip and provides information about additional hardening caused by interactions of fixed slip systems β and active slip systems η, such that h βη is determined by Equation (B2):

$$h_{\beta\eta} = q^{\beta\eta}\left[h_0\left(1-\tau_C^{\eta}/\tau_{sat}\right)^{a}\right] \tag{B2}$$

where h_0, τ_C^{η} and τ_{sat} are, respectively, the reference hardening, the critical shear stress of plane η, and the saturation shear stress. These parameters depend on the crystal structure and the slip system. The parameter a has not a direct physical meaning, but has a direct influence on the development of hardening (typically, $a \geq 1$). The latent hardening parameter, $q_{\beta\eta}$, defines the interaction between system β and η. It is set to 1 if β and η are coplanar, and to 1.4 otherwise [35].

According with the visco-plastic formulation of Asaro and Needleman [36], the shear rate $\dot{\gamma}^{\eta}$ on the system η depends on the resolved shear stress, τ^{η}, and the critical resolved shear stress (CRSS), τ_C^{η}, as stated in Equation (B3).

$$\dot{\gamma}^{\eta} = \dot{\gamma}_0\left|\tau^{\eta} \Big/ \tau_C^{\eta}\right|^{n} sign(\tau^{\eta}) \tag{B3}$$

In Equation (B3), the exponent n is related to strain rate sensitivity, and $\dot{\gamma}_0$ is the reference shear rate. Both parameters are material dependent.

The main purpose of the crystal plasticity simulations in this work is to resolve the development of local stresses and strains depending on the orientation and environment of individual austenite grains in order to elucidate the possibility of the occurrence of variant selection during the bainitic transformation after ausforming. The model described above is very simplistic, but has demonstrated to be effective for the current aim. The presence, motions, and interactions of dislocations are not explicitly identified by the model. Any specific physical contribution to hardening of Geometrical Necessary Dislocations (GNDs) is disregarded by the local crystal plasticity model. The development of mechanical twins may have an influence on the nucleation and growth of bainite plates, as occurs for martensite laths [37]. However, it can be assumed that the stacking fault energy of the material at the deformation temperature of 400 °C is not enough for an extensive development of twinning as the density of twins from unreformed and deformed austenite remains very similar. The formation of mechanically induced martensite or bainite within the austenite grain also contributes to build high stresses in the surroundings [38]. The formation of mechanically induced bainite in this material is likely occurring at this deformation temperature as discussed in [6]. However, up to around 12% deformation at 400 °C, this material follows a behavior than can be described in terms of JC model. This model was formulated for materials with a flow behavior mainly controlled by dislocations. In this regard, low deformation levels were selected to minimize the occurrence of bainitic transformation in the studied microstructures. The resulting local strain after the simulations are produced solely by slip and thus by a markedly shear component, which can give an indication of the preferential direction of bainite laths growth and thus on the development of anisotropic microstructures.

For the calibration of the model, a synthetic microstructure was generated for Damask simulations by the Dream 3D software [13]. This microstructure is representative of the austenite microstructure statistics in terms of grain size distribution and texture obtained from XRD texture measurements, both reported in Ref. [8,11]. This Representative Volume Element (RVE), shown in Fig. B1(a). The JC model, fitted with the parameters in Appendix A, were used to compare the RVE stress–strain curve. Fig. B1(b) shows the results of the parameter calibration process in which simulated curve using the calibration RVE fits reasonably good to Johnson–Cook curve. The resulting material model parameters are shown in Table B1.

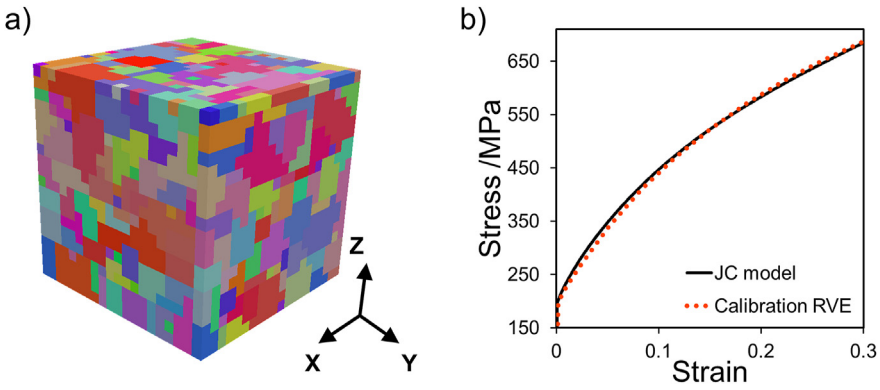

Fig. B1 – (a) RVE used for the calibration of parameters, of dimensions 20 × 20 × 20 voxels^3 (2.5 μm/voxel); (b) Comparison between JC model and compression behavior of the RVE used for the calibration of the parameters.

Table B1 – Crystal plasticity model parameters after calibration.

Parameter	Adopted values for austenite at 400 °C
C_{11}, C_{12}, C_{44}	198 GPa, 125 GPa, 122 GPa
$\dot{\gamma}_0$	1 × 10-6 s^{-1}
n_{slip}	20
$\tau_{C,0}$	64 MPa
τ_{sat}	298 MPa
h_0	479 MPa
a	1.48

REFERENCES

[1] Bhadeshia HKD. Bainite in steels: theory and practice. CRC Press; 2019.

[2] Gong W, Tomota Y, Koo MS, Adachi Y. Effect of ausforming on nanobainite steel. Scripta Mater 2010;63:819–22.

[3] Yi HL, Lee KY, Bhadeshia HKDH. Mechanical stabilisation of retained austenite in δ-TRIP steel. Mater Sci Eng A 2011;528:5900–3.

[4] Shipway PH, Bhadeshia HKDH. Mechanical stabilisation of bainite. Mater Sci Technol 1995;11:1116–28.

[5] Shipway PH, Bhadeshia HKDH. The mechanical stabilisation of Widmanstatten ferrite. Mater Sci Eng A-Str Mater Prop Microstruct Process 1997;223:179–85.

[6] Eres-Castellanos A, Caballero FG, Garcia-Mateo C. Stress or strain induced martensitic and bainitic transformations during ausforming processes. Acta Mater 2020;189:60–72. https://doi.org/10.1016/j.actamat.2020.03.002.

[7] Gong W, Tomota Y, Adachi Y, Paradowska AM, Kelleher JF, Zhang SY. Effects of ausforming temperature on bainite transformation, microstructure and variant selection in nanobainite steel. Acta Mater 2013;61:4142–54. https://doi.org/10.1016/j.actamat.2013.03.041.

[8] Eres-Castellanos A, Morales-Rivas L, Latz A, Caballero FG, Garcia-Mateo C. Effect of ausforming on the anisotropy of low temperature bainitic transformation. Mater Char 2018;145:371–80. https://doi.org/10.1016/j.matchar.2018.08.062.

[9] Miyamoto G, Iwata N, Takayama N, Furuhara T. Variant selection of lath martensite and bainite transformation in low carbon steel by ausforming. J Alloys Compd 2013;577:S528–32. https://doi.org/10.1016/j.jallcom.2011.12.111.

[10] Hase K, Garcia-Mateo C, Bhadeshia H. Bainite formation influenced by large stress. Mater Sci Technol 2004;20:1499–505. https://doi.org/10.1179/026708304X6130.

[11] Eres-Castellanos A, Morales-Rivas L, Jimenez JA, Caballero FG, Garcia-Mateo C. Effect of ausforming on the macro and micro-texture of bainitic microstructures. Metallurg Mat Trans A 2021.

[12] Bachmann F, Hielscher R, Schaeben H. Texture analysis with MTEX–free and open source software toolbox. Solid state phenom, vol. 160. Trans Tech Publ; 2010. p. 63–8.

[13] Groeber MA, Jackson MA. DREAM. 3D: a digital representation environment for the analysis of microstructure in 3D. Integr Mater Manuf Innov 2014;3:5.

[14] Roters F, Eisenlohr P, Kords C, Tjahjanto DD, Diehl M, Raabe D. DAMASK: the Düsseldorf Advanced MAterial Simulation Kit for studying crystal plasticity using an FE based or a spectral numerical solver. Procedia IUTAM 2012;3:3–10.

[15] Nyyssönen T, Peura P, Kuokkala VT. Crystallography, morphology, and martensite transformation of prior austenite in intercritically annealed high-aluminum steel. Metall Mater Trans A Phys Metall Mater Sci 2018. https://doi.org/10.1007/s11661-018-4904-9.

[16] ASTM International. Standard specification for silicon nitride bearing balls. 2018. https://doi.org/10.1520/F2094_F2094M-18A.

[17] Systèmes D. Abaqus 6.10 online documentation. Abaqus User Subroutines Ref Man; 2010.

[18] Wang X, Li H, Chandrashekhara K, Rummel SA, Lekakh S, Van Aken DC, et al. Inverse finite element modeling of the barreling effect on experimental stress-strain curve for high temperature steel compression test. J Mater Process Technol 2017;243:465–73. https://doi.org/10.1016/j.jmatprotec.2017.01.012.

[19] Shirzadi AA, Abreu H, Pocock L, Klob?ar D, Withers PJ, Bhadeshia HKDH. Bainite orientation in plastically deformed austenite. Int J Mater Res 2009;100:40–5.

[20] Olson GB, Cohen M. Stress-assisted isothermal martensitic transformation: application to TRIP steels. Metall Trans A 1982;13:1907–14.

[21] Chatterjee S, Wang HS, Yang JR, Bhadeshia HKDH. Mechanical stabilisation of austenite. Mater Sci Technol 2006;22:641–4.

[22] Singh SB, Bhadeshia HKDH. Estimation of bainite plate-thickness in low-alloy steels. Mater Sci Eng A 1998;245:72–9.

[23] Pous-Romero H, Bhadeshia H. Coalesced martensite in pressure vessel steels. J Press Vessel Technol Trans ASME 2014;136. https://doi.org/10.1115/1.4026192.

[24] Pak J, Suh DW, Bhadeshia HKDH. Promoting the coalescence of bainite platelets. Scripta Mater 2012;66:951–3. https://doi.org/10.1016/j.scriptamat.2012.02.041.
[25] Humbert M, Wagner F, Liu WP, Esling C, Bunge HJ. Proc. 8th Int. Conf. on 'Textures of materials'. 1988.
[26] Sum M, Jonas JJ. A dislocation reaction model for variant selection during the austenite-to-martensite transformation. Texture, Stress, Microstruct 1999;31:187–215.
[27] Bishop JFW, Hill R. XLVI. A theory of the plastic distortion of a polycrystalline aggregate under combined stresses. London, Edinburgh. Dublin Philos Mag J Sci 1951;42:414–27.
[28] Bokros JC, Parker ER. The mechanism of the martensite burst transformation in Fe-Ni single crystals. Acta Metall 1963;11:1291–301.
[29] Wittridge NJ, Jonas JJ, Root JH. A dislocation-based model for variant selection during the γ-to-α′ transformation. Metall Mater Trans 2001;32:889.
[30] Durlu TN, Christian JW. Effect of prior deformation on the martensite burst transformation in single crystals of an Fe-Ni-C alloy. Acta Metall 1979;27:663–6.
[31] Chiba T, Miyamoto G, Furuhara T. Comparison of variant selection between lenticular and lath martensite transformed from deformed austenite. ISIJ Int 2013;53:915–9.
[32] Miyamoto G, Iwata N, Takayama N, Furuhara T. Quantitative analysis of variant selection in ausformed lath martensite. Acta Mater 2012;60:1139–48. https://doi.org/10.1016/j.actamat.2011.11.018.
[33] Tripathy H, Hajra RN, Sudha C, Raju S, Saibaba S. Measurement of high temperature elastic moduli of an 18Cr-9Ni-2.95 Cu-0.58 Nb-0.1 C (Wt%) austenitic stainless steel. AIP Conf. Proc., vol. 1951. AIP Publishing LLC; 2018. p. 20009.
[34] Khatak H, Raj B. Corrosion of austenitic stainless steels: mechanism, mitigation and monitoring. Woodhead publishing; 2002.
[35] Maresca F, Kouznetsova VG, Geers MGD. On the role of interlath retained austenite in the deformation of lath martensite. Model Simulat Mater Sci Eng 2014;22:45011.
[36] Asaro RJ, Needleman A. Overview no. 42 texture development and strain hardening in rate dependent polycrystals. Acta Metall 1985;33:923–53.
[37] Mao C, Liu C, Yu L, Li H, Liu Y. Discontinuous lath martensite transformation and its relationship with annealing twin of parent austenite and cooling rate in low carbon RAFM steel. Mater Des 2021;197:109252.
[38] Deng XT, Cheng M, Zhang SH, Song HW, Taha MA. Residual stresses and martensite transformation in AISI 304 austenitic stainless steel. Mater Res Express 2018;6:16503.